Journal of Industrial and Engineering Chemistry 77 (2019) 76–82

Contents lists available at ScienceDirect

Journal of Industrial and Engineering Chemistry

journal homepage: www.elsevier.com/locate/jiec

New synthesis strategy for hollow NiO nanofibers with interstitial nanovoids prepared via electrospinning using camphene for anodes of lithium-ion batteries

Jang Hyeok Oh[a,1], Min Su Jo[a,1], Sang Mun Jeong[b], Chungyeon Cho[c], Yun Chan Kang[d,*], Jung Sang Cho[a,*]

[a] *Department of Engineering Chemistry, Chungbuk National University, Gaesin-Dong, Seowon-Gu, Cheongju, 361-763, Republic of Korea*
[b] *Department of Chemical Engineering, Chungbuk National University, Gaesin-Dong, Seowon-Gu, Cheongju, 361-763, Republic of Korea*
[c] *Department of Carbon Convergence Engineering, College of Engineering, Wonkwang University, Iksan, Jeonbuk, 54538, South Korea*
[d] *Department of Materials Science and Engineering, Korea University, Anam-Dong, Seongbuk-Gu, Seoul, 136-713, Republic of Korea*

ARTICLE INFO

Article history:
Received 11 December 2018
Received in revised form 3 April 2019
Accepted 9 April 2019
Available online 18 April 2019

Keywords:
Hollow structure
Electrospinning
NiO
Camphene
Anodes

ABSTRACT

This paper introduces a new synthesis strategy suitable for the one-step synthesis of hollow 1-dimension nanostructures and highly desirable for the simple preparation of well-defined hollow nanostructures with high product yields using camphene. The viscosity gradient of the jet during the electrospinning results in the inward movement of the camphene. Subsequently, the sublimation of camphene generates internal hollow space without further processing. The resulting nanofibers exhibit a reversible discharge capacity of 956 mA h g^{-1} after 400 cycles when applied as anodes for lithium-ion batteries. The discharge capacities of the nanofibers are 1050, 1024, 937, 796, 643, and 483 mA h g^{-1} at current densities of 0.5, 1.5, 3.0, 5.0, 7.0, and 10.0 A g^{-1}, respectively. The NiO nanofibers with hollow structure show high structural stability and shorten the Li^+-ion diffusion pathway during cycles, which resulted in excellent lithium-ion storage properties.

Introduction

In recent years, the development of technology for controlling the structure, size, and morphology of the nanomaterials is one of the key goals for powder synthesis [1–5]. As a unique class of structured materials, hollow nanostructures have attracted considerable interest owing to their intrinsic characteristics, such as their thin shell, large internal void, doubled surface area, and robust stability [6–9]. Therefore, hollow nanomaterials have been used in various fields, including drug delivery, chemical storage, gas sensors, catalysis, and energy storage [10–13].

With regard to the anode materials of lithium-ion battery (LIB) applications, hollow one-dimensional (1D) nanostructures with a high aspect ratio effectively accommodate the severe volumetric expansions of active materials upon cycling and prevent the self-aggregation of the nanoscale subunits, thus leading to improved capacity retention [14–17]. Additionally, the enhanced contact surface between the active material and the electrolyte promotes the electrochemical reaction, which induces high rate performance of LIBs [18–21]. Moreover, the 1D geometry having direct channels for efficient electron transport along the longitudinal direction allows the materials to interact efficiently with Li^+ ions, resulting in a high power density of LIBs [22–25]. Therefore, hollow 1D nanomaterials with various compositions have been prepared via numerous strategies, such as emulsion electrospinning, coaxial electrospinning, template methods, and heating processes for the Ostwald ripening effect [26–45]. (summarized in Table S1)

For example, Paik et al. synthesized nitridated TiO_2 hollow nanofibers via a coaxial electrospinning method and subsequent nitridation treatment. This structure exhibited a discharge capacity of 156 mA h g^{-1} at 0.2 C and capacity retention of 100% after 100 cycles when used as an anode material for LIBs [34]. Lu et al. prepared carbon-coated Fe_3O_4 nanotubes with a hierarchical porous structure by removing the MoO_3 template from an MoO_3@FeOOH hybrid. The nanotubes exhibited a high reversible capacity of 1020 mA h g^{-1} and high cycling performance, with capacity retention of 103% after 150 cycles [38]. Additionally, Kim et al. fabricated manganese-cobalt oxide hollow nanofibers via electrospinning and subsequent calcination in air. A high heating

---

[*] Corresponding authors.
E-mail addresses: yckang@korea.ac.kr (Y.C. Kang), jscho@cbnu.ac.kr (J.S. Cho).
[1] These authors contributed equally to this work.

https://doi.org/10.1016/j.jiec.2019.04.021

rate caused fast combustion, resulting in hollow fibers. The hollow $MnCo_2O_4$ nanofibers exhibited a discharge capacity of 997 mA h g^{-1} and a Coulombic efficiency (CE) of 98% after 50 cycles [45]. Even though many hollowing strategies have been proposed, camphene has not been used as a pore generator in the electrospinning process for the synthesis of hollow 1D nanofibers. Although An et al. prepared SnO_2 hollow nanofibers by heat-treatment of as-spun fibers containing camphene, the camphene was not applied as a pore generator [46]. Therefore, as-spun fibers have totally solid structure, which is due to the similar vapor pressures of DMF and camphene, no viscosity gradient arose for the contents in the jet. To demonstrate this, we will investigate in detail the effect of differences in vapor pressure between solvents on nanostructure geometry in this study. Generally, the camphene, which has a melting point of approximately 45 °C has been used as a freezing vehicle in the freeze-casting method for obtaining pores in bio-ceramic structures because it can be frozen and easily sublimed near room temperature [47,48].

The new method introduced in this study is suitable for the one-step synthesis of hollow 1D nanostructures and is highly desirable for the simple preparation of well-defined hollow nanostructures with high product yields. The new method, therefore, overcomes the limitations of the previous hollow strategies such as complications arising from the complex interplay between factors such as the miscibility, viscosity, and the interfacial tension, etc. between the solutions used. Moreover, the unintended destruction of hollow nanostructures during template removal, such as template methods, can be prevented. In this study, compared with EtOH, the low vapor pressure of camphene and the phase separation from polyvinylpyrrolidone (PVP) induces the assembly of camphene at the center of the 1D structure during electrospinning. The sublimation of camphene in the center generates a well-defined internal hollow space in the structure after the spinning process, without further processing. In this study, NiO was selected as the first candidate anode material for applying this strategy because of its low cost, environmental friendless, and large theoretical capacity of 718 mA h g^{-1} in LIBs [49,50]. The detailed formation mechanism of the hollow 1D nanostructures via the facile strategy using camphene was examined in detail, and the effects of the morphological features on the electrochemical properties as an anode material in LIBs were studied. The facile synthesis strategy introduced in this study is expected to improve the properties of traditional metal oxides for various applications that require hollow 1D nanostructures.

Experimental

Sample preparation

Hollow NiO nanofibers were prepared via electrospinning and subsequent heat treatment. For the electrospinning, the spinning solution was prepared by dissolving 0.5 g of $Ni(NO_3)_2{\cdot}6H_2O$ (Daejung, 97%), 3.0 g of PVP (Alfa Aesar, Mw: 1,300,000), 7.0 g of camphene (Acros Organics, 75%), and 2.0 mL of acetic acid (Daejung Chemicals and Metals, 99.7%) in 50 mL of ethanol (Duksan, 99.9%) with vigorous stirring overnight. The prepared solution was loaded into a plastic syringe equipped with a 25-gague stainless-steel nozzle at a flow rate of 1.0 mL h^{-1}. The solution was subsequently ejected and electrospun onto a drum collector covered with aluminum, while the rotation of the drum was maintained at 180 rpm. During the electrospinning process, the applied voltage between the collector and the syringe tip was 20 kV. The distance between the tip and the collector was maintained at 20 cm. The resultant as-spun nanofibers were stabilized at 150 °C for 24 h in an air atmosphere. NiO nanofibers with a hollow structure were obtained after heat treatment at 350 °C for 3 h in an air atmosphere. As a comparison sample, NiO nanofibers with a solid structure were prepared via heat treatment of the as-spun nanofibers obtained from the aforementioned spinning solution without camphene and oxidized at 600 °C for 5 h.

Characterizations

The morphology of the prepared nanofibers was observed using field-emission scanning electron microscopy (SEM, Zeiss, ULTRA PLUS, ZEISS) and field-emission transmission electron microscopy (TEM, JEOL, JEM-2100 F). Their crystal structures were investigated using X-ray diffractometry (XRD, D8 Discover with GADDS, Bruker)

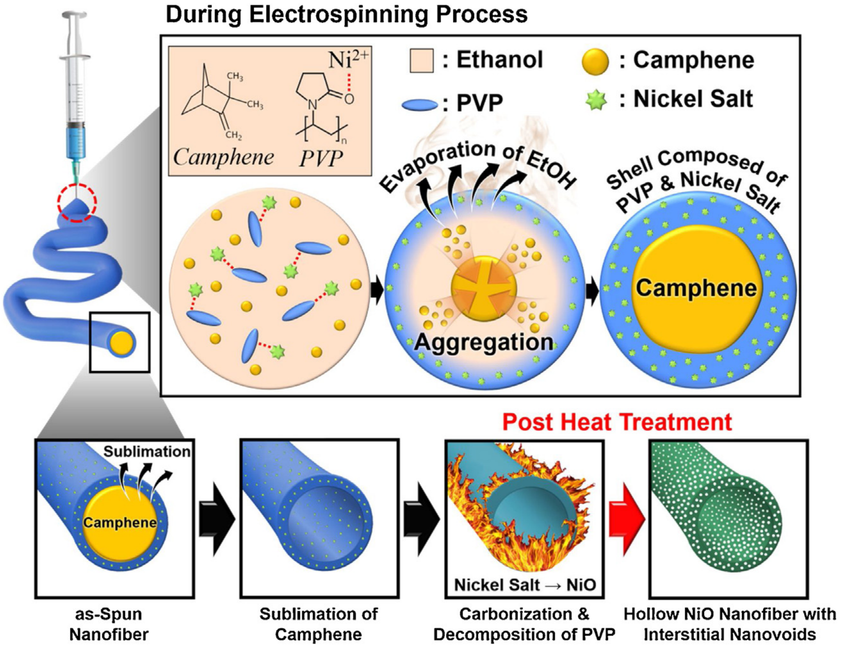

Scheme 1. Formation mechanism of the hollow NiO nanofibers using camphene via the facile two-step strategy.

with Cu K_α radiation ($\lambda = 1.5418$ Å). X-ray photoelectron spectroscopy (XPS, Thermo Scientific K-Alpha) with focused monochromatic Al K_α at 12 kV and 20 mA was used to determine the compositions of the specimens. The surface areas of the samples were measured using the Brunauer-Emmett-Teller (BET) method, with N_2 as the adsorbate gas. Thermogravimetric (TG) analysis was conducted using a Pyris 1 Thermogravimetric Analyzer (Perkin Elmer) within a temperature range of 25–700 °C at a heating rate of 10 °C min^{-1}, in an air atmosphere.

Electrochemical measurements

The electrochemical properties of the NiO nanofibers were analyzed by constructing 2032-type coin cells. The anode was prepared by mixing the active material, carbon black (Super-P), and sodium carboxymethyl cellulose at a weight ratio of 7:2:1. Lithium metal and a microporous polypropylene film were used as the counter electrode and separator, respectively. The electrolyte was 1 M $LiPF_6$ in a 1:1 (vol/vol) mixture of fluoroethylene carbonate and dimethyl carbonate. The cells were assembled in a glove box in an argon atmosphere. The discharge and charge characteristics of the samples were investigated via cycling in the potential range of 0.001–3.0 V. Cyclic voltammograms (CVs) were measured at a scan rate of 0.1 mV S^{-1} between 0.001 and 3.0 V. The charge-discharge behavior of the samples was tested at current densities ranging from 0.5–10.0 A g^{-1} within the same potential window of 0.001–3.0 V. Electrochemical impedance spectroscopy (EIS) was performed on the electrode in the frequency range of 100 kHz–0.01 Hz.

Results and discussion

Well-defined hollow NiO nanofibers were prepared using camphene via the facile two-step strategy described in Scheme 1. After dissolution in EtOH, the precursors PVP, nickel salt, and camphene were separated into continuous and dispersed phases owing to their differences in hydrophobicity. Here, benefiting from the lactam groups of PVP, the Ni^{2+} ion of nickel salt can be well-coordinated with PVP molecular chains in a solution [51]. During the electrospinning, the EtOH solvent having a high vapor pressure (5.83 kPa at 20 °C) evaporated rapidly from the surface of the jet, forming a shell composed of PVP and nickel salt on the jet surface while the camphene molecules (vapor pressure at 20 °C was 0.33 kPa) migrated to the center of the jet [52]. As the surface solidification proceeded, the viscosity of the outer layer of jet increased more rapidly than that of the deeper layer, yielding a viscosity gradient from the outer layer to the inner layer. This resulted in the inward movement of the camphene molecules and, furthermore, their mergence. Finally, the merged camphene molecules in the center sublimated under ambient conditions, yielding a well-defined hollow inner space in the nanofibers without further heat treatment. During the heat treatment, NiO nanograins were formed from the nickel salt, and concurrently, PVP was carbonized and then decomposed into CO_2 gas, yielding loosely packed hollow NiO nanofibers with interstitial nanovoids.

The as-spun nanofibers obtained by applying the facile mechanism are shown in Fig. 1. The nanofibers exhibited a smooth nanofiber surface and had a mean diameter of 600 nm. As shown the inset image of Fig. 1a, a 120-nm-thick shell layer containing a hollow inner space was identified after spinning, even though no further processing was performed on the fractured nanofiber. During the spinning, the viscosity gradient from the outer layer to the inner layer due to the evaporation of EtOH solvent from the jet surface resulted in the inward movement of camphene and its mergence. Subsequently, the camphene sublimated owing to its high sublimation feature after spinning, yielding the hollow inner space in the PVP-nickel salt composite nanofibers. The XRD pattern confirms that the as-spun nanofibers had an amorphous-like phase comprising PVP and nickel salt (Fig. 1b). The complete sublimation of camphene in the structure was confirmed by the absence of the functional groups of camphene from the FT-IR spectrum shown in Fig. S1. To confirm the effect of the vapor-pressure difference between the solvents on the nanostructured geometry, dimethylformamide (DMF) with a low vapor pressure of 0.36 kPa at 20 °C was used as a counter solvent with camphene [53], in which the difference of the vapor pressures was only 0.03 kPa. After electrospinning, solid nanofibers were obtained, as shown in Fig. S2. Owing to the similar vapor pressures of DMF and camphene, no viscosity gradient arose for the contents in the jet. Therefore, phase separation of camphene and aggregation at the center of the jet were not achieved.

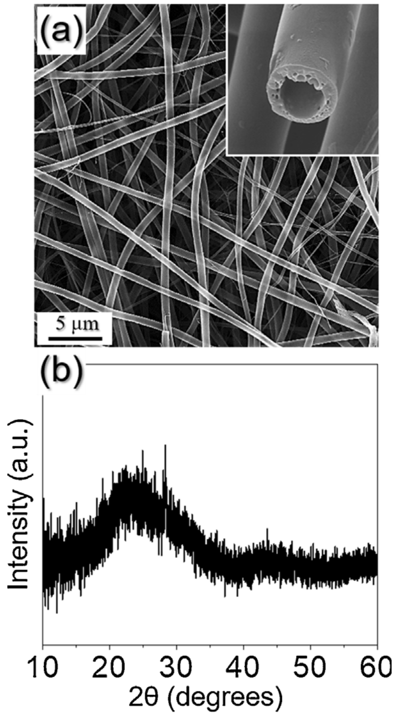

Fig. 1. Morphologies and XRD pattern of the $Ni(NO_3)_2 \cdot 6H_2O$/PVP composite nanofibers prepared using camphene by electrospinning: (a) FE-SEM image, (b) XRD pattern.

To obtain the well-defined hollow NiO nanofibers, simple heat treatment of the as-spun nanofibers was performed at 350 °C in an air atmosphere. The resulting nanofiber morphology is shown in Fig. 2. The overall 1D nanostructure was well-maintained even after heat treatment, as shown in Fig. 2a. Moreover, the fractured nanofiber surface showed that the nanofibers had a well-defined hollow inner space in the longitudinal direction of the structure. The diameter of the nanofibers decreased to 200 nm owing to the thermal contraction during the heat treatment. Additionally, the thickness of the shell layer was approximately 10 nm. According to the XRD results shown in Fig. 2c, the nanofiber had a cubic crystal-structured pure NiO phase [54,55]. By applying the Scherrer equation to the (200) NiO crystal lattice, the mean crystallite size of the NiO nanofibers was calculated as 6.1 nm. Additionally, clear mesopores between the NiO nanograins composing the shell layer are observed in the high-resolution TEM (HR-TEM) image of Fig. 2d. During heat treatment, the PVP in the composite was carbonized, which prevented the growth of NiO nanograins surrounded by carbon. Then, the PVP decomposed into CO_2 gas, forming mesopores between the nanograins, as indicated by the arrows

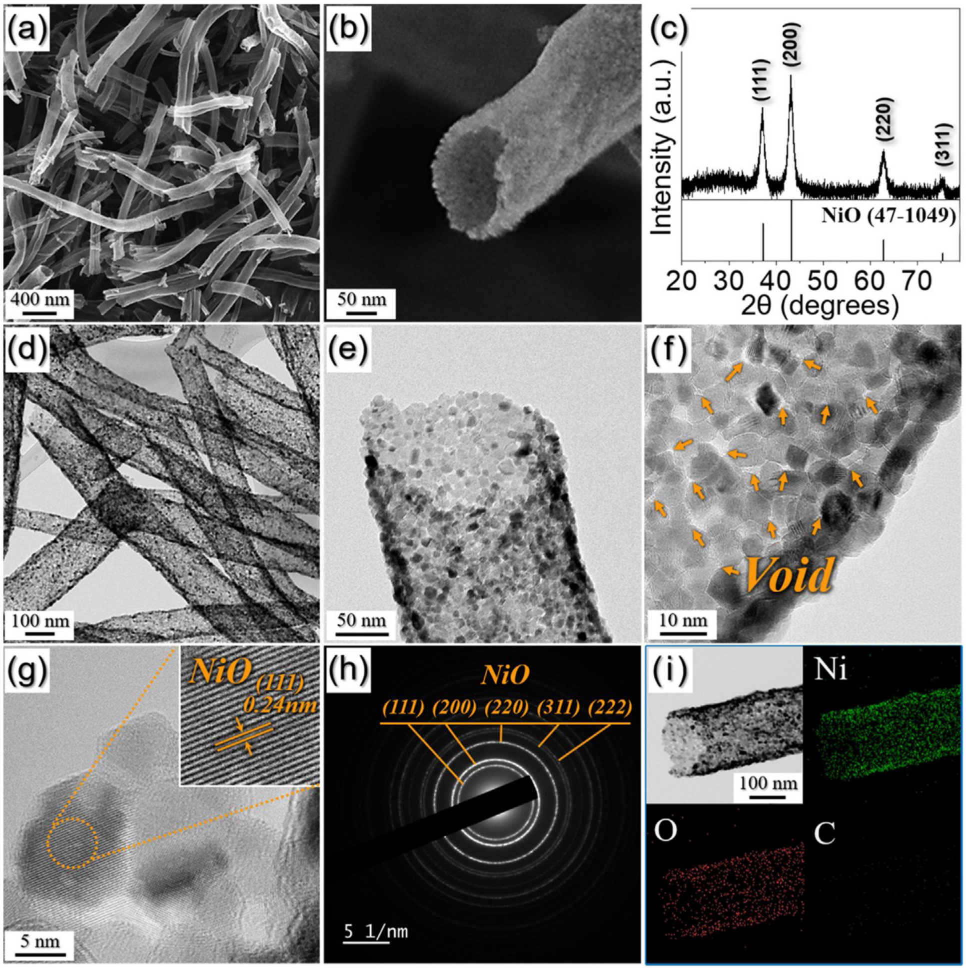

Fig. 2. Morphologies, XRD pattern, SAED pattern, and elemental mapping images of the hollow NiO nanofiber: (a, b) FE-SEM images, (c) XRD pattern, (d, e) TEM images, (f, g) HR-TEM images, (h) SAED pattern, and (i) elemental mapping images.

in Fig. 2f. These mesopores facilitated the penetration of the electrolyte in the structure during cycling, promoting the electrochemical reactions. The HR-TEM image shows that the shell was composed of NiO nanograins ranging in size from 5 to 6 nm, which is consistent with the crystallite size calculated via XRD. In the inset image of Fig. 2g, the lattice fringes separated by 0.24 nm correspond to the (111) plane of cubic NiO [56]. The selected-area electron diffraction (SAED) pattern shown in Fig. 2h confirms the formation of the NiO phase, which is in agreement with the XRD results shown in Fig. 2c. The dot-mapping images of the hollow NiO nanofibers indicate that the NiO nanograins were uniformly formed as a shell layer and that the PVP was completely decomposed during the heat treatment.

The phase information of the hollow NiO nanofibers was investigated using XPS, as shown in Fig. 3. The spectrum was deconvoluted by Gaussian curves to estimate the proportions of the phases. In Fig. 3a, the survey spectrum reveals the presence of the elements nickel and oxygen in the structure. The high-resolution Ni 2p spectrum (Fig. 3b) clearly indicates Ni^{2+} peaks at 854.2 and 871.5 eV and Ni^{3+} peaks at 855.8 and 873.2 eV, along with their satellite peaks [57–59]. The Ni_2O_3 phase is attributed to the formation of oxygen-rich nickel oxide, which was presumably due to the burning of carbon during the heat treatment [60,61]. However, because the pure NiO phase was confirmed in the XRD, it is assumed that the amount of oxygen-rich nickel oxide was negligible. Additionally, in the O 1s spectrum, two binding energy

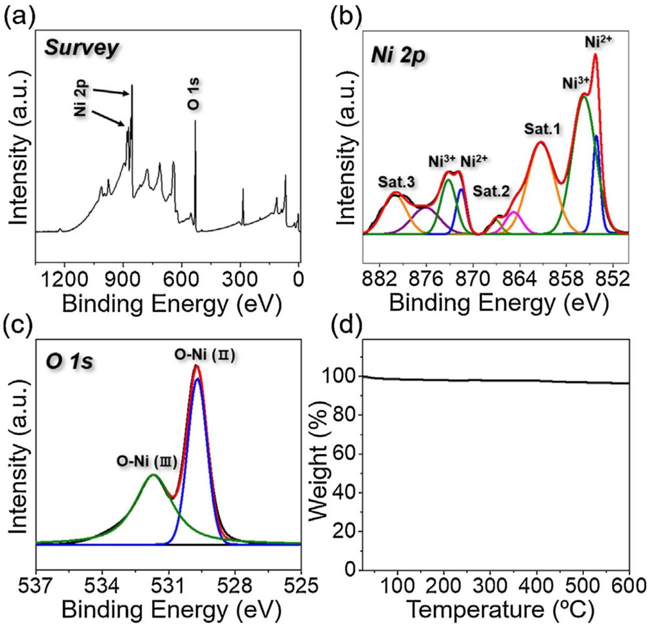

Fig. 3. XPS spectra and TGA curve of the hollow NiO nanofiber: (a) wide-scan XPS spectrum, (b) XPS spectrum of Ni 2p, (c) XPS spectrum of O 1s, and (d) TGA curve.

peaks were observed at 529.8 and 531.5 eV, as shown in Fig. 3c. The peak at 529.8 eV is ascribed to the typical metal-oxygen bond of Ni-O [62]. The additional peak at 531.5 eV was due to oxygen-rich nickel oxide [43]. According to the characteristic binding energy values of nickel and oxygen, we can confirm that NiO was successfully formed during the heat treatment. The weight loss was negligible according to the TG curve (Fig. 3d), implying that the structure was composed of a pure NiO phase without carbon.

Solid NiO nanofibers were prepared for comparison of the Li^+-ion storage properties with the hollow nanofibers. For this, as-spun nanofibers (Fig. S3) obtained from the solution containing nickel salt and PVP without camphene were heat-treated at 600 °C in an air atmosphere. The complete removal of the carbon formed from PVP in the structure was achieved above 600 °C due to the solid structure. The morphology of the resulting nanofibers is shown in Fig. 4. The SEM image of the fractured surface in Fig. 4b confirms the solid nanostructure. The nanofiber was compactly composed of NiO nanograins, as shown in Fig. 4c and d. The lattice fringes, as well as the SAED and XRD patterns in Fig. 4d–f, confirm the formation of cubic-structured NiO [54,55]. The mean crystallite size of the solid NiO nanofibers was calculated as 25.2 nm by applying the Scherrer equation to the (200) lattice, which is higher than that of hollow NiO nanofibers. According to the dot-mapping images, the solid NiO nanofibers did not contain carbon. The BET surface areas of the hollow and solid NiO nanofibers shown in Fig. S4 were 61 and 4.8 $m^2\ g^{-1}$, respectively. The hollow inner space and the interstitial nanovoids between the NiO nanograins induced a large BET surface area of the hollow NiO nanofibers.

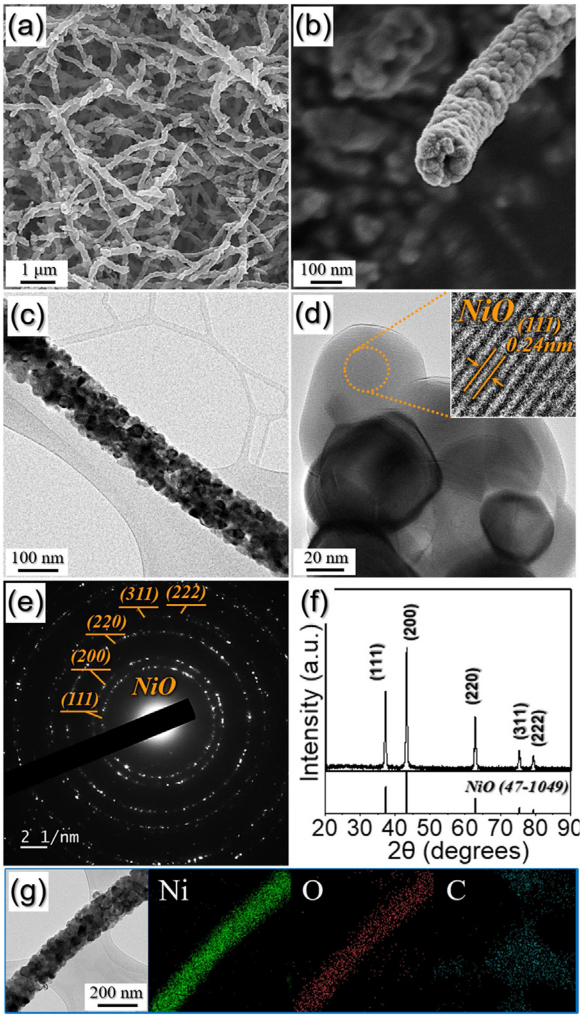

Fig. 4. Morphologies, SAED pattern, XRD pattern and elemental mapping images of the solid NiO nanofibers: (a, b) FE-SEM images, (c) TEM image, (d) HR-TEM image, (e) SAED pattern, (f) XRD pattern, and (g) elemental mapping images.

The Li^+-ion storage properties of the hollow NiO nanofibers as an anode material were compared with those of solid NiO nanofibers, as shown in Fig. 5. The CV of the hollow NiO nanofibers for the first five cycles at a scan rate of 0.1 mV s^{-1} over the potential range of 0.001–3.0 V (vs Li^+/Li) is shown in Fig. 5a. In the first cathodic scan, the initial peak around 0.89 V as a shoulder is attributed to the imperfection of the NiO nanograins formed by the low heat-treatment temperature of 350 °C [63]. The following peak at 0.48 V was due to the electrolyte decomposition to form the solid electrolyte interphase (SEI) layer and the reduction of NiO to nickel, accompanied by the formation of amorphous Li_2O [63–65]. After the second cycle, the reduction peaks were shifted to a higher potential of 0.98 V owing to the formation of an ultrafine NiO nanocrystal during the cycle [63–65]. In the anodic scan, two broad reversible peaks at 1.45 and 2.23 V were observed, which were due to the decomposition of the SEI layer and the subsequent oxidation of nickel to NiO, along with the decomposition of Li_2O [63–65]. The good overlapping of the cathodic/anodic peaks from the second cycle onward reveals their excellent reversibility during the repeated lithiation/delithiation processes. The CV curves of the solid NiO nanofibers are similar to those of the hollow ones (Fig. S5).

The initial charge–discharge profiles of the hollow and solid NiO nanofibers at a high current density of 2.0 A g^{-1} are shown in Fig. 5b. The profiles of the samples are consistent with the CV results. The initial discharge capacities of the hollow and solid NiO nanofibers were 1174 and 898 mA h g^{-1}, respectively, and their corresponding initial CEs were 72.9% and 64.4%, respectively. Compared with the solid nanofibers, the hollow NiO nanofibers shortened the Li^+-ion diffusion pathway and reduced the resistance of the electrolyte, which prevented the polarization in the active material, leading to a significantly higher initial discharge capacity. The cycling performances of both nanofibers at a current

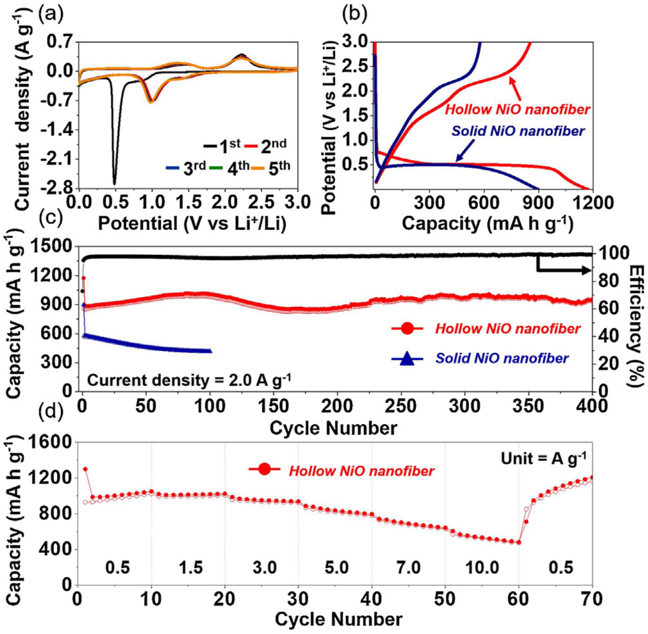

Fig. 5. Electrochemical properties of the hollow and solid NiO nanofibers: (a) CV curves of the hollow NiO nanofibers, (b) initial discharge-charge profiles (c) cycling performances at a current density of 2.0 A g^{-1}, and (d) rate performance of the hollow NiO nanofibers.

density of 2.0 A g^{-1} are shown in Fig. 5c. The hollow NiO nanofibers exhibited excellent cycling performance even at a high current density. The hollow NiO nanofibers delivered a reversible specific discharge capacity of 956 mA h g^{-1} after 400 cycles, and the corresponding CE was steadily maintained at >98.7%. The hollow architecture effectively accommodated the severe volume variation of NiO nanograins upon cycling and prevented the self-aggregation of the nanoscale subunits, leading to improved capacity retention even at the high current density. In contrast, a continuous decrease in capacity to 416 mA h g^{-1} after 100 cycles was confirmed in the solid NiO nanofibers because of the failure to withstand the large volume variations during the repeated cycles.

The hollow NiO nanofibers also exhibited an excellent rate property, as shown in Fig. 5d. The discharge capacities of the hollow NiO nanofibers were 1050, 1024, 937, 796, 643, and 483 mA h g^{-1} at current densities of 0.5, 1.5, 3.0, 5.0, 7.0, and 10.0 A g^{-1}, respectively. The hollow nanostructure and the interstitial nanovoids between the NiO nanograins provided easy accessibility of the electrolyte into the electrode, promoting the Li^+-ion diffusion kinetics. Furthermore, the 1D geometry having direct channels for efficient electron transport along the longitudinal direction allowed the active materials to interact more efficiently with Li^+ ions, yielding the high rate performance of the hollow NiO nanofibers. When the current density was returned to 0.5 A g^{-1}, the discharge capacity recovered well to 1208 mA h g^{-1}, implying that the Li^+-ion storage performance of the hollow NiO nanofibers was not degraded after operation at the high current densities. The electrochemical properties of the product prepared in this study was also compared with other NiO materials previously reported in Table S2. Compared with the previously reported materials, hollow NiO nanofibers exhibited the enhanced cycling stability at high current density.

EIS was performed to investigate the Li^+-ion storage kinetics of the hollow NiO nanofibers compared with those of solid NiO nanofibers. Nyquist plots of the samples before and after the 1st and 50th cycles were obtained via deconvolution with a Randle-type equivalent-circuit model, as shown in Fig. 6. The medium-frequency semicircles in the Nyquist plots are attributed to the charge-transfer resistance (R_{ct}) between the active material and the electrolyte [66,67]. The R_{ct} value of the hollow NiO nanofibers was 62 Ω, which is significantly lower than that of the solid NiO nanofibers (481 Ω) before cycling, as shown in Fig. 6a. The hollow nanostructure with ultrafine nanocrystals resulted in the low R_{ct} of the sample. The R_{ct} values for both types of nanofibers decreased after the first cycle owing to the formation of ultrafine nanocrystals during the first discharge and charge processes [68]. After 50 cycles, the hollow NiO nanofibers maintained their low R_{ct} value (8 Ω), indicating the high structural stability of the sample during the repeated Li^+-ion lithiation/delithiation processes, as shown in Fig. 6b. The hollow space and the interstitial nanovoids in the shell layer improved the structural stability of the sample. Additionally, the easy accessibility of the electrolyte into the electrode and the short diffusion length for Li^+ ions reduced the charge-transfer resistance. However, the R_{ct} value of the solid NiO nanofibers significantly increased to 21 Ω after 50 cycles owing to the structural destruction during cycling.

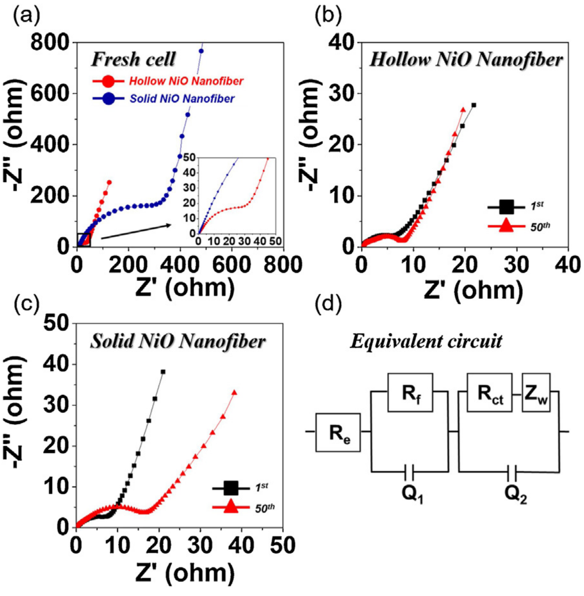

Fig. 6. Nyquist impedance plots of the hollow and solid NiO nanofibers: (a) before cycling, (b) after cycling of the hollow NiO nanofibers, (c) after cycling of the solid NiO nanofibers, and (d) equivalent circuit model used for AC impedance fitting.

Conclusions

A new strategy suitable for the one-step synthesis of hollow 1D nanostructures using camphene via electrospinning was introduced. During electrospinning, EtOH evaporated rapidly from the surface of the jet, yielding a gel shell composed of PVP and nickel salt on the jet surface, while the camphene molecules migrated to the center of the jet. The viscosity gradient from the outer layer to the inner layer resulted in the inward movement of the camphene molecules. The sublimation of camphene in the center yielded a well-defined hollow inner space in the nanofibers. Subsequent heat treatment resulted in the formation of loosely packed hollow NiO nanofibers with interstitial nanovoids. The hollow nanofibers exhibited superior electrochemical properties for Li^+-ion storage owing to their improved the structural stability and shortened the Li^+-ion diffusion path, allowing the penetration of the electrolyte into the structure during repeated Li^+ lithiation/delithiation processes. The facile synthesis strategy introduced in this study is expected to improve the properties of traditional metal oxides for various applications that require hollow 1D nanostructures.

Acknowledgements

This work was supported by the National Research Foundation of Korea (NRF) grant funded by the Korea government (MSIP) (NRF-2018R1A4A1024691, NRF-2017M1A2A2087577, NRF-2018R1D1A3B07042514).

References

[1] M. Guo, H. Chen, S. Wang, S. Dai, L.-X. Ding, H. Wang, J. Alloys Compd. 687 (2016) 746.
[2] S.Y. Jeong, S.-K. Park, Y.C. Kang, J.S. Cho, Chem. Eng. J. 351 (2018) 559.
[3] A.D. Roberts, X. Li, H. Zhang, Chem. Soc. Rev. 43 (2014) 4341.
[4] S.L. Zhang, B.Y. Guan, H.B. Wu, X.W.D. Lou, Nano-Micro Lett. 10 (2018) 44.
[5] C. Zhu, X. Xia, J. Liu, Z. Fan, D. Chao, H. Zhang, H.J. Fan, Nano Energy 4 (2014) 105.
[6] L. Balcells, C. Martínez-Boubeta, J. Cisneros-Ferna'ndez, K. Simeonidis, B. Bozzo, J. Oro'-Sole, N. Bague's, J. Arbiol, N. Mestres, B. Martínez, ACS Appl. Mater. Interfaces 8 (2016) 28599.
[7] S.-K. Park, S.H. Yang, Y.C. Kang, Chem. Eng. J. 349 (2018) 214.
[8] C.C. Nguyen, N.N. Vu, T.-O. Do, J. Mater. Chem. A 3 (2015) 18345.
[9] Y.M. Chen, L. Zhen, X.W. Lou, Angew. Chem. Int. Ed. 127 (2015) 10667.
[10] D. Cai, L. Ding, S. Wang, Z. Li, M. Zhu, H. Wang, Electrochim. Acta 139 (2014) 96.
[11] J.S. Cho, J.-S. Park, Y.C. Kang, Sci. Rep. 6 (2016) 38933.
[12] F.-X. Ma, H. Hu, H.B. Wu, C.-Y. Xu, Z. Xu, L. Zhen, X.W.D. Lou, Adv. Mater. 27 (2015) 4097.
[13] C. Sun, J. Yang, X. Rui, W. Zhang, Q. Yan, P. Chen, F. Huo, W. Huang, X. Dong, J. Mater. Chem. A 3 (2015) 8483.
[14] Z. Han, B. Wang, X. Liu, G. Wang, H. Wang, J. Bai, J. Mater. Sci. 53 (2018) 8445.
[15] J. Sun, C. Lv, F. Lv, S. Chen, D. Li, Z. Guo, W. Han, D. Yang, S. Guo, ACS Nano 11 (2017) 6186.
[16] J. Xiang, X.-Y. Yu, U. Paik, J. Power Sources 329 (2016) 190.
[17] G. Yang, X. Xu, W. Yan, H. Yang, S. Ding, Electrochim. Acta 137 (2014) 462.

[18] L. Li, S. Peng, J.K.Y. Lee, D. Ji, M. Srinivasan, S. Ramakrishna, Nano Energy 39 (2017) 111.
[19] J. Luo, X. Xia, Y. Luo, C. Guan, J. Liu, X. Qi, C.F. Ng, T. Yu, H. Zhang, H.J. Fan, Adv. Energy Mater 3 (2013) 737.
[20] J. Yang, Y. Guo, Y. Zhang, C. Sun, Q. Yan, X. Dong, Nanotechnology 27 (2016) 365401.
[21] L. Zhang, S. Zhu, H. Cao, L. Hou, C. Yuan, Chem. Eur. J. 21 (2015) 10771.
[22] Y. Chen, Y. Wang, H. Yang, H. Gan, X. Cai, X. Guo, B. Xu, M. Lü, A. Yuan, Ceram. Int. 43 (2017) 9945.
[23] J.S. Cho, Y.J. Hong, Y.C. Kang, ACS Nano 9 (2015) 4026.
[24] C. Guan, X. Wang, Q. Zhang, Z. Fan, H. Zhang, H.J. Fan, Nano Lett. 14 (2014) 4852.
[25] K.-X. Wang, X.-H. Li, J.-S. Chen, Adv. Mater. 27 (2015) 527.
[26] B. Ren, M. Fan, Q. Liu, J. Wang, D. Song, X. Bai, Electrochim. Acta 92 (2013) 197.
[27] T. Wang, J. Wei, H. Shi, M. Zhou, Y. Zhang, Q. Chen, Z. Zhang, Physica. E 86 (2017) 103.
[28] W. Zeng, W. Chen, Z. Li, H. Zhang, T. Li, Mater. Res. Bull. 65 (2015) 157.
[29] T. Yang, B. Lu, Phys. Chem. Chem. Phys. 16 (2014) 4115.
[30] M. Zhang, X. Huang, H. Xin, D. Li, Y. Zhao, L. Shi, Y. Lin, J. Yu, Z. Yu, C. Zhu, J. Xu, App. Surf. Sci. 473 (2019) 352.
[31] J. Chen, Y. Song, Y. Sheng, M. Chang, X. Xie, M.M. Abualrejal, H. Guan, Z. shi, H. Zou, J. Alloys Compd. 716 (2017) 144.
[32] L. Shen, Y. Yao, T. Wang, L. Jia, S. Chen, IOP Conf. Ser. Mater. Sci. Eng. 439 (2018) 022017.
[33] Y. Zhou, W. Song, L. Zhang, S. Tao, J. Mater. Chem. A 6 (26) (2018) 12298.
[34] H. Han, T. Song, J.-Y. Bae, L.F. Nazar, H. Kim, U. Paik, Energy Environ. Sci. 4 (2011) 4532.
[35] Y. Sun, R.B. Sills, X. Hu, Z.W. Seh, X. Xiao, H. Xu, W. Luo, H. Jin, Y. Xin, T. Li, Z. Zhang, J. Zhou, W. Cai, Y. Huang, Y. Cui, Nano lett. 15 (6) (2015) 3899.
[36] Y.B. Yin, J.J. Xu, Q.C. Liu, X.B. Zhang, Adv. Mater. 28 (34) (2016) 7494.
[37] S.P. Adhikari, H.R. Pant, H.M. Mousa, J. Lee, H.J. Kim, C.H. Park, C.S. Kim, J. Ind. Eng. Chem. 35 (2016) 75.
[38] F. Han, L. Ma, Q. Sun, C. Lei, A. Lu, Nano Res. 7 (2014) 1706.
[39] X. Luo, Z. Pan, F. Pei, Z. Jin, K. Miao, P. Yang, H. Qian, Q. Chen, G. Feng, J. Ind. Eng. Chem. 59 (2018) 410.
[40] Y. Jiang, F. Li, Y. Liu, Y. Hong, P. Liu, L. Ni, J. Ind. Eng. Chem. 41 (2016) 130.
[41] Z. Sun, Y. Zhang, X. Deng, J. Li, C. Xiong, J. Ind. Eng. Chem. 18 (1) (2012) 92.
[42] C. Jia, H.S. Chen, P. Yang, J. Ind. Eng. Chem. 58 (2018) 278.
[43] H. Zhu, D. Yu, Zhang S, J. Chen, W. Wu, M. Wan, L. Wang, M. Zhang, M. Du, Small 13 (26) (2017)1700468.
[44] M. Wan, H. Zhu, S. Zhang, H. Jin, Y. Wen, L. Wang, M. Zhang, M. Du, Electrochim. Acta 279 (2018) 301.
[45] S.M. Hwang, S.Y. Kim, J.-G. Kim, K.J. Kim, J.-W. Lee, M.-S. Park, Y.-J. Kim, M. Shahabuddin, Y. Yamauchi, J.H. Kim, Nanoscale 7 (2015) 8351.
[46] B.R. Koo, S.T. Oh, H.J. Ahn, Mater. Lett. 178 (2016) 288.
[47] E.-J. Lee, Y.-H. Koh, B.-H. Yoon, H.-E. Kim, H.-W. Kim, Mater. Lett. 61 (2007) 2270.
[48] A. Macchetta, I.G. Turner, C.R. Bowen, Acta Biomater. 5 (2009) 1319.
[49] Y. Li, X. Li, Z. Wang, H. Guo, T. Li, Ceram. Int. 42 (2016) 14565.
[50] M.M. Rahman, S.-L. Chou, C. Zhong, J.-Z. Wang, D. Wexler, H.-K. Liu, Solid State Ionics 180 (2010) 1646.
[51] H. Xue, X. Mu, J. Tang, X. Fan, H. Gong, T. Wang, J. He, Y. Yamauchi, J. Mater. Chem. A 4 (2016) 9106.
[52] O.Y. Kurapova, V.G. Konakov, S.N. Golubev, V.M. Ushakov, I.Y. Archakov, Rev. Adv. Mater. Sci. 32 (2012) 112.
[53] M.S. Jo, G.D. Park, Y.C. Kang, J.S. Cho, Nanoscale 10 (2018) 13539.
[54] S.H. Choi, Y.C. Kang, ACS Appl. Mater. Interfaces 6 (2014) 2312.
[55] W. Wang, Y. Liu, C. Xu, C. Zheng, G. Wang, Chem. Phys. Lett. 362 (2002) 119.
[56] J.S. Cho, S.Y. Lee, H.S. Ju, Y.C. Kang, ACS Appl. Mater. Interfaces 7 (2015) 25641.
[57] A. Habrioux, I. Abidat, C. Canaff, C. Morais, C. Comminges, T.W. Napporn, K.B. Kokoh, ECS Trans. 77 (2017) 15.
[58] J. Li, C. Chen, Mater. Res. Express 5 (2018) 015502.
[59] Q.H. Lu, R. Huang, L.S. Wang, Z.G. Wu, C. Li, Q. Luo, S.Y. Zuo, J. Li, D.L. Peng, G.L. Han, P.X. Yan, J. Magn. Magn. Mater. 394 (2015) 253.
[60] J.-S. Park, J.S. Cho, Y.C. Kang, J. Power Sources 379 (2018) 278.
[61] Y. Zhu, H. Guo, Y. Wu, C. Cao, S. Tao, Z. Wu, J. Mater. Chem. A 2 (2014) 7904.
[62] S.H. Oh, J.-S. Park, M.S. Jo, Y.C. Kang, J.S. Cho, Chem. Eng. J. 347 (2018) 889.
[63] J.S. Cho, J.M. Won, J.-H. Lee, Y.C. Kang, Nanoscale 7 (2015) 19620.
[64] X.H. Huang, J.P. Tu, C.Q. Zhang, X.T. Chen, Y.F. Yuan, H.M. Wu, Electrochim. Acta 52 (2007) 4177.
[65] H.S. Jadhav, G.M. Thorat, J. Mun, J.G. Seo, J. Power Sources 302 (2016) 13.
[66] J.S. Cho, J.-S. Park, K.M. Jeon, Y.C. Kang, J. Mater. Chem. A 5 (2017) 10632.
[67] G. Gao, L. Shi, S. Lu, T. Gao, Z. Li, Y. Gao, S. Ding, Dalton Trans. 47 (2018) 3521.
[68] J.H. Kim, Y.C. Kang, Nano Res. 10 (2017) 3178.